

Full length article

The role of aluminium in chemical and phase segregation in a TRIP-assisted dual phase steel

B.L. Ennis^{a, b, *}, E. Jimenez-Melero^{b, c}, R. Mostert^a, B. Santillana^a, P.D. Lee^{b, d}^a Tata Steel Research and Development, 1970 CA IJmuiden, The Netherlands^b The School of Materials, University of Manchester, Oxford Road, Manchester, M13 9PL, UK^c Dalton Cumbrian Facility, Westlakes Science and Technology Park, Moor Row, CA24 3HA, UK^d Manchester X-Ray Imaging Facility, Research Complex at Harwell, RAL, Didcot, OX11 0FA, UK

ARTICLE INFO

Article history:

Received 29 March 2016

Received in revised form

27 May 2016

Accepted 27 May 2016

Available online 6 June 2016

Keywords:

Steel

Casting

Chemical segregation

Phase transformation

Thermo-mechanical processing

ABSTRACT

In this work we demonstrate that micro-segregation patterns of alloying elements present in a high-strength TRIP-assisted DP steel after casting are retained in the microstructure throughout processing, and lead to anisotropy (banding) in the final microstructure. In particular, we have assessed the role of Al on the chemical segregation of Mn, Cr and Si during casting, and their impact on the phase transformations occurring during thermo-mechanical processing of the as-cast material. We have derived the elemental partition coefficients, based on the experimentally determined dendrite spacing and chemical profiles in the as-cast structure, and used them to derive the local austenite-to-ferrite transformation temperature. Our cellular automaton methodology to simulate phase transformations allows reliable prediction of the formation or suppression of banding in the intermediate and final microstructures for different heating or cooling rates. Our results reveal that aluminium exerts the largest individual effect of the substitutional elements on the formation of banding in these steels. Controlling micro-segregation during solidification in advanced high-strength multiphase steels is therefore critical for obtaining homogeneous mechanical properties in the final product, as it controls the phase transformations occurring during thermo-mechanical processing and therefore the final microstructure.

Crown Copyright © 2016 Published by Elsevier Ltd on behalf of Acta Materialia Inc. This is an open access article under the CC BY license (<http://creativecommons.org/licenses/by/4.0/>).

1. Introduction

Increasing demands of weight reduction and improved safety in the automotive industry have led to the ongoing development of advanced high strength steel grades with increased ductility and microstructural complexity *e.g.* Transformation and Twinning Induced Plasticity steels (TRIP and TWIP respectively) [1,2], Quench and Partitioning (Q&P) steels [3–6] and their derivatives, such as TRIP-assisted dual phase steels. In most of these steels, the local carbon content is controlled during processing to retain a significant amount of metastable austenite at room temperature. The retained austenite confers the steel with enhanced ductility, as a result of the mechanically induced transformation of austenite to martensite. In order to suppress carbide formation during quenching, significant additions of other alloying elements such as

silicon and aluminium are employed [2,7,8]. Silicon is most commonly added as it not only suppresses carbide formation but also contributes to solid solution strengthening; as does manganese. Due to problems during hot-rolling, coating and welding arising from the formation of tenacious Si-based surface oxides, silicon is increasingly being partially or completely replaced by aluminium in high strength-high ductility steels [9–12]. This current practice requires increasing amounts of manganese to compensate for the loss of solid solution strengthening. The trend towards increasingly complex and finer microstructures or increased amounts of retained austenite, requires delicate control of the microstructure and interactions of the alloying elements during processing to achieve the desired structure and stability and, hence, mechanical properties.

Limited solid solubility of alloying elements in steel leads to segregation during casting. During solidification, solute is partitioned between the solid and liquid to either enrich or deplete interdendritic regions. This naturally leads to variations in composition on the scale of micrometres, *i.e.* micro-segregation. Macro-segregation, however, refers to chemical variations over

* Corresponding author. Tata Steel Research and Development, 1970 CA IJmuiden, The Netherlands.

E-mail address: bernard.ennis@tatasteel.com (B.L. Ennis).

length scales approaching the dimensions of the casting, which for large ingots may be of the order of centimetres or metres [13]. At any given temperature, for an alloy with bulk solute concentration C_0 , the solute concentration in the solid may be designated as C_S and that of the liquid as C_L . Redistribution or partitioning of solute is then defined using the equilibrium partitioning coefficient [13]:

$$k = \frac{C_S}{C_L} \quad (1)$$

This forms the basis for the Scheil-Gulliver equation [14] from which the composition of the liquid during solidification can be calculated, thus:

$$C_L = C_0(f_L)^{k-1} \quad (2)$$

And for the solid, thus:

$$C_S = kC_0(1 - f_S)^{k-1} \quad (3)$$

Where f_S and f_L are the weight fractions in the solid and liquid respectively.

Since the solidus and liquidus lines bounding a specific solidification region are approximately straight, k is constant within that (limited) composition range. For many systems, k has a value less than unity *i.e.* the solute is rejected from the solid as it forms and accumulates in the liquid. Average values of k for typical alloying additions in steel obtained from the literature are shown in Table 1. The lack of long-range order in the liquid portion allows a greater uptake of solute than in the crystalline solid [13]. As solidification progresses, the concentration of solute in the liquid increases due to rejection from the solid into the liquid phase, with the highest concentration of solutes in the last portion of liquid to freeze.

Considerable research effort has been devoted to investigating the effect of carbon, manganese and, to a lesser extent, chromium and silicon on the dendrite arm spacing [15–18], microscopic [19–21] and macroscopic segregation [22–24], partitioning during phase transformations [25–30] and on banding [22,31] in steels. There has to date been no systematic study of the role of aluminium segregation in these processes in modern automotive high strength steels. In fact, on the basis of the partition coefficients in Table 1, it would appear that aluminium would not segregate significantly during solidification, although this is almost certainly due to the residual levels of aluminium (< 0.04 wt%) reported in the study [21]. The occurrence of Mn and Al macro-segregation has been recently reported in a medium-Mn multiphase steel [32], but Al seems to homogenise after thermo-mechanical treatment in that case, and the observed martensite-austenite micro-bands were attributed only to the Mn segregation.

The aim of this work is (1) to determine the potential role of aluminium as an alloying addition on the partitioning of the other solute elements in multi-phase steels and (2) to establish the link between chemical segregation in the as-cast structure with the phase transformations taking place during subsequent processing steps that may result in the occurrence of banding in the final

microstructure. Our initial hypothesis is that interdendritic chemical segregation remains after casting and, in particularly in the case of aluminium, is instrumental in causing banding throughout the manufacturing process.

2. Experimental

2.1. Material production

The steel under investigation is a continuously-cast TRIP assisted dual phase steel with the composition given in Table 2. The material is produced via a continuous casting route, followed by hot-rolling (HR), cold-rolling (CR) and continuous annealing. Samples from industrial production material were taken after casting and also after cold-rolling and annealing (CRA) for the experiments and analysis outlined in this work.

Blocks of 75 mm in height (1/3 of the original slab height of 225 mm) were removed from the centre-line of the as-cast (AC) slab, as this is the most common section for the appearance of both chemical macro- and micro-segregation due to (a) increased dendrite arm spacing as a result of slower cooling rates and (b) solute enrichment of the final solidification zone [33]. The blocks were first forged to a thickness of 35 mm, before being reheated to 1250 °C for 30 min and subsequently hot-rolled in six deformation passes to the final thickness of 3.4 mm, see Fig. 1. The temperature after the final reduction was 900 °C and the microstructure at this step is comprised completely of austenite. Different cooling trajectories were subsequently applied aimed to promote (slow cooling rate) or suppress (fast cooling rate) banding as predicted by the cellular-automaton model developed by Bos et al. [34,35], see Section 3.2 for details. Slow cooled samples were first allowed to cool in air to 700 °C, followed by oven cooling to room temperature at 0.2 °C/s; the fast cooled samples were water quenched to 600 °C on a run-out table delivering a continuous flow rate of water to achieve a constant cooling rate of 100 °C/s, this was followed by oven cooling to room temperature at 0.2 °C/s.

The samples were subsequently cold-rolled to 1 mm thickness and annealed in the ferrite (α) + austenite (γ) region, followed by a bainite isothermal holding treatment at 400 °C for 60 s. According to Caballero et al., successful suppression of banding during hot-rolling can be undone during subsequent heat-treatments if the heating rate up to the two-phase region is too low [36]. To avoid, or effectuate the occurrence of banding, the heating rate during annealing was adapted to mirror the cooling rate in the hot-rolling process, within the practical limits of industrial annealing lines. The main process parameters are given in Fig. 1. It should be noted that the total deformation from rolling reductions of material produced in the laboratory (95%) is less than that for the samples taken from the production route (99%), see Table 3.

2.2. Structural characterisation

Microstructural analysis was performed by light optical microscopy and scanning electron microscopy (Zeiss Ultra 55 FEG-SEM). Chemical etchants were used to reveal the microstructure in the HR condition (5% Nital) and in the CRA condition (LePera reagent). Dendrite arm spacing was measured on SEM images using Fiji image analysis software [37]. Images were converted from grey

Table 1
Reported values of the equilibrium partition coefficients for common alloying elements in steel.

Element	Valid composition range, wt%	k	Reference
Mn	1.4–1.5	0.71	[21,25]
Al	0.03–0.05	1.02	[21]
Si	0.3–0.4	0.63	[21]
Cr	–	0.33	[25]

Table 2
Chemical composition of the studied TRIP-assisted dual phase steel grade in wt%.

C	Mn	Al	Si	Cr	Fe
0.15	2.05	0.58	0.42	0.40	Bal.

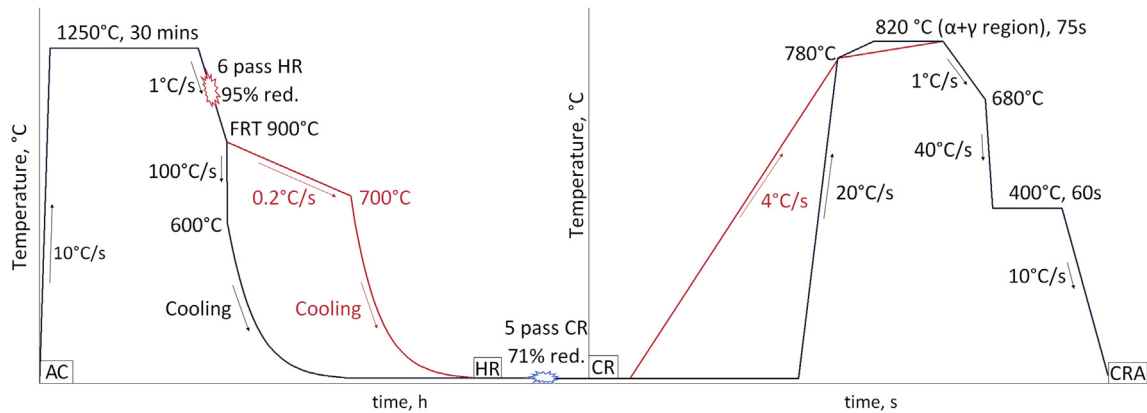


Fig. 1. Schematic diagram of the processing conditions for promoting (red) and suppressing (black) banding. Hot-rolling (including reheating) and cold-rolling are shown (left) on different time-temperature scales to the subsequent continuous annealing cycle (right). AC = as-cast, FRT = finishing rolling temperature, HR = as hot-rolled, CR = as cold-rolled, CRA = as cold-rolled and annealed. (For interpretation of the references to colour in this figure legend, the reader is referred to the web version of this article.)

Table 3
Comparison of rolling reductions and the predicted and measured through-process dendrite arm spacing and average distance between segregation bands from industrial production and laboratory samples.

Process step	As cast		Hot rolled		Cold-rolled and annealed	
	Production	Laboratory ^a	Production	Laboratory ^a	Production	Laboratory
Sample thickness, mm	225	75	3.0	3.4	1.0	1.0
Rolling reduction, %	n/a	95	99	95	66	71
Predicted dendrite arm spacing, μm	370–400	17.2 \pm 1.5	5.0 \pm 0.2	12.1 \pm 4	1.7 \pm 0.1	5.1 \pm 0.5
Measured distance between segregation and second phase bands, μm	380 \pm 36	6.2 \pm 0.8	no data	12.1 \pm 4	1.9 \pm 0.3	6.2 \pm 0.8

^a As-cast thickness of samples hot- and cold-rolled in the laboratory was 75 mm.

scale to binary and subsequent noise removal was carried out using the built-in, single iteration “Renji Entropy” threshold filter to remove dark outliers with an x and y radius of 3 pixels, corresponding to 3 μm . Analysis of band and segregation spacing was carried out using a peak-to-peak analysis of the line scans performed on hot- and cold-rolled microstructures and virtual line scan analysis of data parallel to a primary dendrite arm of the area maps in the as-cast structure, with a minimum line intersection of 20 secondary arms.

Mapping of alloying elements was carried out using a JEOL JSM-7001F SEM equipped with two 30 mm² SDD detectors (Thermo Fisher Scientific) and a NORAN-System7 with NSS.3.3 software. The accelerating voltage was 15 kV, and the beam current in the focused probe was 16 nA. Area scans were performed on the as-cast structure over a total area of 7.5 \times 7.5 mm² with a step size of 10 μm . Higher resolution scans of 1 \times 0.75 mm² with a step size of 2.5 μm were also performed on the dendrites and interdendritic region. Line scans were performed over a series of sections in the as-cold rolled structure over a total length of 160 μm with a nominal step size of 1 μm and a finer step size of 0.5 μm across the central portion (70–90 μm).

Based on the assumption that any partitioning of elements with $k < 1$ would manifest itself in higher average alloy content in the final liquid to solidify, partition coefficients were calculated using a bi-modal Gaussian analysis of the distribution from the element maps of the as cast structure with binning at 0.01 wt %. The partition coefficient is then the ratio of the higher to lower modal concentration.

3. Computations

3.1. Phase diagram and partitioning coefficient

Calculation of the pseudo-binary equilibrium diagram of Fe-

0.15C-2Mn-0.4Cr-0.4Si-[0–2]Al was carried out using the Phase Diagram module of the FactSage programme version 6.4 in combination with the FSSStel database, release March 2015 [38]. Incremental and cumulative partition coefficients were calculated in the Equilib module of FactSage and the same FSSStel database using Scheil-Gulliver cooling conditions with temperature step of 5 $^{\circ}\text{C}$ and assuming (a) equilibrium partitioning of carbon and (b) continuous cooling rate of 0.5 $^{\circ}\text{C}/\text{s}$.

3.2. Numerical modelling

Another numerical technique used to simulate phase transformations is the cellular automaton (CA) stochastic-based method where rules are applied that in the limit are solutions of the governing differential equations [33]. Although these techniques do not capture the same level of detail as e.g. phase field modelling, it is possible to simulate grain structures over much larger simulation domains than with the phase field method. Bos et al. have developed a 3D CA model which can be used to calculate the effect of local composition on the austenite to ferrite transformation during hot-rolling [34] and during continuous annealing after cold-rolling [35]. This aids the understanding of the mechanism by which segregation drives the tendency towards banding in multiphase steels.

Based on the partition coefficients it is possible to calculate the critical austenite-to ferrite transformation temperature, Ae_3 , in the bulk material, in the bands and at the centre-line. In this way differences in transformation temperature (ΔAe_3) between segregated and non-segregated areas can be calculated and applied to a wave function representing the compositional periodicity, including a maximum concentration at the position of the centre-line, according to:

$$\Delta Ae_3 = Ae_3[band] - Ae_3[bulk] \tag{4}$$

3.3. Analytical approximation of Ae_3 transformation temperature

In order to model the effect of segregation on band formation, it is necessary to have an adequate function for the effect of elemental distribution on the transformation behaviour. In this way the banding process is modelled by assigning local chemistries based on the partition coefficients and calculating the local transformation temperatures. One such function, derived by Andrews [39], is given as:

$$Ae_3(^{\circ}C) = 910 - 25C_{Mn} + 60C_{Si} - 11C_{Cr} \tag{5}$$

Where Ae_3 temperature is expressed in $^{\circ}C$ and concentrations in wt %.

This function does not deal reliably with Al and C, so it was necessary to derive a new function to include these terms. Numerical analysis was carried out on model alloys generated from MTDATA [40] and resulted in the following polynomial function, which is described in more detail in Ref. [41]:

$$Ae_3(^{\circ}C) = \sum c_{XkYmZn} X^k Y^m Z^n \tag{6}$$

Where Ae_3 temperature is expressed in $^{\circ}C$ and concentrations in wt %.

All terms consist of a parameter c_{XkYmZn} and are the product of at most three chemical elements X, Y and Z to the power k, m and n respectively, where X, Y and Z are the elements C, Mn, Cr, Si, and Al and k, m and n are integers between 0 and 6. The number of non-zero terms is rather large and do not give additional physical insight; the values of the polynomial coefficients are therefore given in Table 2 in the accompanying Data in Brief article [41].

3.4. Multi-component diffusion

Multi-component diffusion was calculated using calculated using Thermo-Calc and DICTRA in combination with thermodynamic TCFE7 and mobility MOBFE2 databases [42,43]. The calculation was carried out using two equi-axed, quaternary Fe-C-Mn-Al grains with a single linear interface, see Fig. 2a. The grain length was 50 μm , being representative of the length scale over which diffusion must operate during homogenisation. A 60 point, non-linear mesh ($r_{high} = 1.1$, $r_{low} = 0.9$) was chosen to ensure a higher

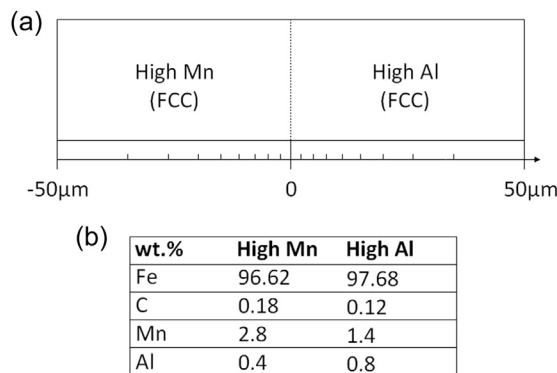


Fig. 2. (a) Linear cell model with Mn and Al segregated areas as used in the DICTRA simulation. The spatial grid is defined in terms of a geometric series with a high density of grid points close to the interface. (b) Initial chemical composition of the phases used in the simulation.

definition of the region close to the interface. Two chemical compositions were chosen based upon the product of the base composition and the average partitioning coefficients of Al and Mn, see Fig. 2b. In accordance with the experimental observations, the Al and Mn are inversely enriched/depleted. Carbon is assumed to partition preferentially to the Mn-rich phase, this being the final fcc phase present during solidification, see Section 5.1. The compositional gradients were described using the Heaviside function.

Step calculations were carried out whereby the maximum diffusion gradient occurs across the interface, thereby inducing the highest mobility potential. This is however not realistic for conditions within a segregated dendrite where there is no sharply defined chemical boundary: in that case, simulations with a linear composition gradient are more appropriate. All calculations (both step and linear) were carried out at 1250 $^{\circ}C$, where both grains would be fully austenitic. The initial time step was set at 1×10^{-7} s; this value was also chosen to be the smallest incremental time step. The calculation finished in all cases at 1×10^6 s.

4. Results

4.1. Casting

EPMA mapping was carried out close to the centre-line of the industrially produced continuously cast slab used in this study. The resultant elemental maps for Al, Si and Mn clearly show the correlation in the concentration profiles of these three elements at the position of the secondary dendrite arms, see Fig. 3. Mn and Si are locally enriched in the interdendritic region, whereas Al shows the opposite trend.

The dendrite arm spacing (DAS) was calculated using the model developed by El-Bealy and Thomas [16], who demonstrated that the primary and secondary dendrite arm spacings in steel are determined by the local cooling rate combined with the carbon content. The measured values of dendrite arm spacing in the as-cast structure, and the associated chemical segregation between the arms, are in good agreement with the values obtained from this model, see in Table 3. It should however be noted that at very low cooling rates, primary and secondary dendrite arm spacings are almost identical, which introduces uncertainty in their identification.

4.2. Thermo-mechanical processing

The CA model was applied using the wave function as previously described in two different conditions to either promote or suppress banding. The process parameters for the first case were: slow cooling (2 $^{\circ}C/s$) after hot-rolling to a high coiling temperature (700 $^{\circ}C$) followed by a low heating rate (4 $^{\circ}C/s$) to the annealing temperature. To suppress banding the parameters were amended thus: fast cooling (100 $^{\circ}C/s$) after hot-rolling to a low coiling temperature (600 $^{\circ}C$) and fast heating rate (20 $^{\circ}C/s$) to the annealing temperature.

The HR microstructures as predicted by the model are shown in Fig. 4a and c for the banded and non-banded conditions respectively alongside those obtained from the experimental work, Fig. 4b and d respectively. The HR microstructures are almost identical to the predicted microstructure with relatively few thick and widely spaced pearlite bands (dark etching phase), especially at the centre-line, sandwiched between ferrite bands (light etching phase). By way of contrast, the microstructure of the fast cooled (100 $^{\circ}C/s$), low coiling temperature (600 $^{\circ}C$) microstructure has a finer grain size (4.3 μm as opposed to 8.4 μm in the previous case), the ferrite and pearlite are much more evenly distributed. Although banding is still evident, the thick centre-line band is much less visible than in

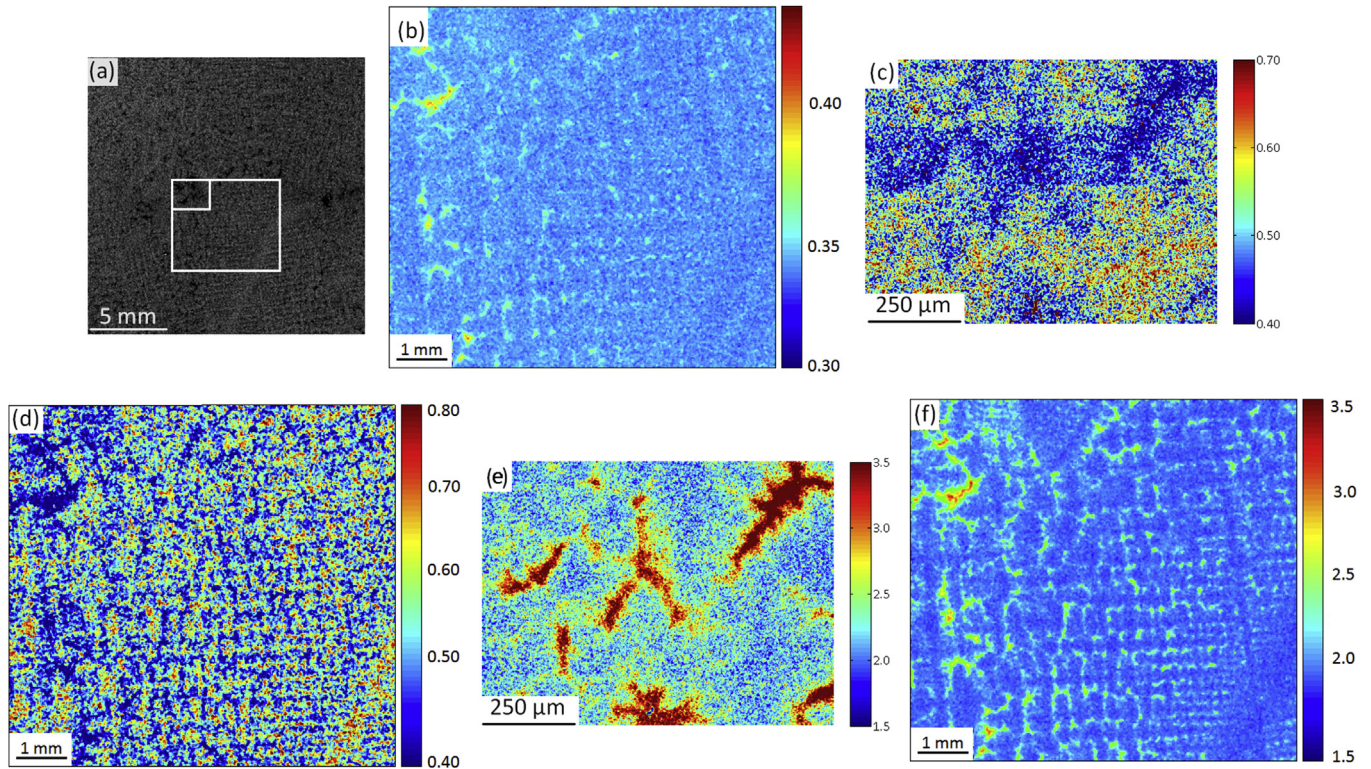


Fig. 3. (a) Back-scattered electron image of the as-cast structure generated in an industrial production line, together with of the distributions of (b) Si (c, d) Al and (e, f) Mn. Images (b), (d) and (f) show large scale EPMA maps ($18 \times 18 \text{ mm}^2$, step size $10 \mu\text{m}$) which reveal the dendritic structure. Images (c) and (e) show higher resolution EDS maps ($1 \times 1 \text{ mm}^2$, step size $2.5 \mu\text{m}$) of the interdendritic region highlighted in (a).

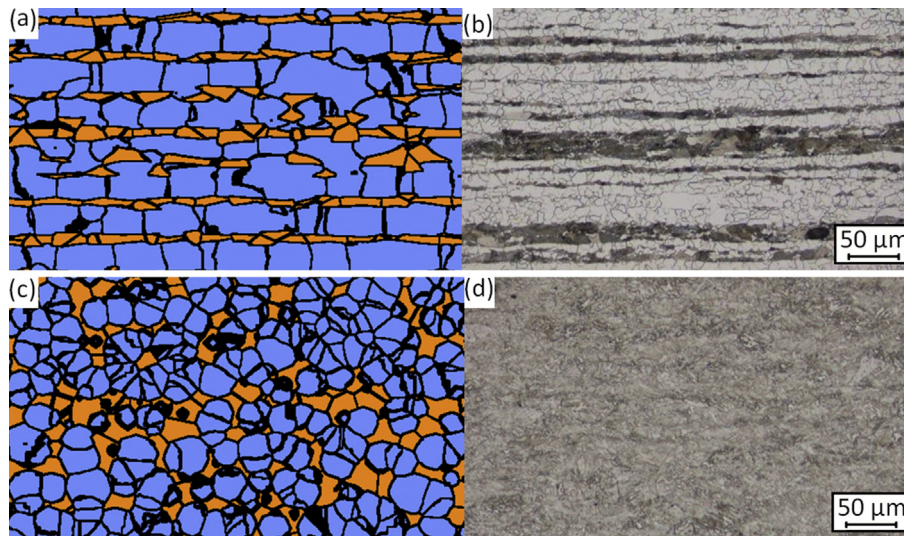


Fig. 4. The microstructures predicted by the CA model in the HR condition for process conditions to (a) promote or (c) suppress the formation of banding are compared to micrographs of the observed structure as etched in 5% Nital (b and d, respectively), see text.

the slow cooled microstructure.

The samples were further cold-rolled and annealed according to the process conditions, see Fig. 1, whereby the heating rate was chosen to either promote (slow heating, $4 \text{ }^\circ\text{C/s}$) or suppress banding (fast heating, $20 \text{ }^\circ\text{C/s}$). To simulate the effect of cold-rolling in the model, the HR microstructure from the model is scaled prior to application of the annealing step. The size in the vertical direction is reduced and in the horizontal direction (the rolling direction) is

increased in the same ratio (60%), resulting in elongated grains aligned parallel to the rolling direction.

The resultant CRA microstructures as predicted by the model are shown in Fig. 5a and c for the banded and non-banded condition respectively and those obtained experimentally are shown in Fig. 5b and d. The CRA microstructure is comprised of a ferrite matrix with a second phase which is actually comprised of martensite and retained austenite, although it is not possible to

differentiate these two phases using light microscopy. Retained austenite is obtained by carbon enrichment during cooling from the intercritical temperature through ferrite re-transformation (to a limited extent) and mainly through bainite formation during isothermal holding. This can also result in a low fraction (less than 5 vol. %) of bainite being present in the microstructure associated with the retained austenite. Not all of the austenite is sufficiently enriched in carbon to remain stable at room temperature. For that reason a fraction of the austenite transforms to martensite during the quenching step after the isothermal bainite holding time. It is clear that the processing aimed at reducing banding has resulted in a finer grain size and significantly reduced centre-line banding, although some orientation is still visible in the second phase microstructure.

Fig. 6 shows the microstructure of production CRA material, which consists of ferrite and a strongly banded second phase. The microstructure shows significant banding, not only at the centre-line, but also throughout the entire microstructure. By superimposing the chemical composition obtained from line scans onto the microstructure (compare Fig. 6a and b), it is evident that there is not only Mn segregation at the centre-line, as would be expected from the literature, but also a strong counter-segregation of Al. The peak across the centre-line band is the strongest, but this pattern is also observed in all of the second phase bands in the microstructure. This follows the same trend as previously observed in the cast microstructure: the periodicity of this measurement is strongly suggestive that the chemical segregation observed in the final CRA microstructure has its origins in the casting structure.

By simple application of the rolling reduction to the DAS measured in the as-cast structure, it is therefore possible to predict the spacing of bands in the final CRA microstructure resulting from chemical segregation. Table 3 gives a comparison of the predicted spacing (based on the dendrite arm spacings obtained using the El-Bealy-Thomas model) and the actual values of segregation bands measured in production and laboratory material. There is a clear correlation between the presence of interdendritic segregation and the occurrence of banding in the intermediate HR and final CRA microstructure. This is particularly evident when comparing the values for CRA material from the laboratory and from production which came from the same cast feedstock, but with less reduction being applied to the laboratory material, which was sectioned from the centre of the cast slab, see Table 3.

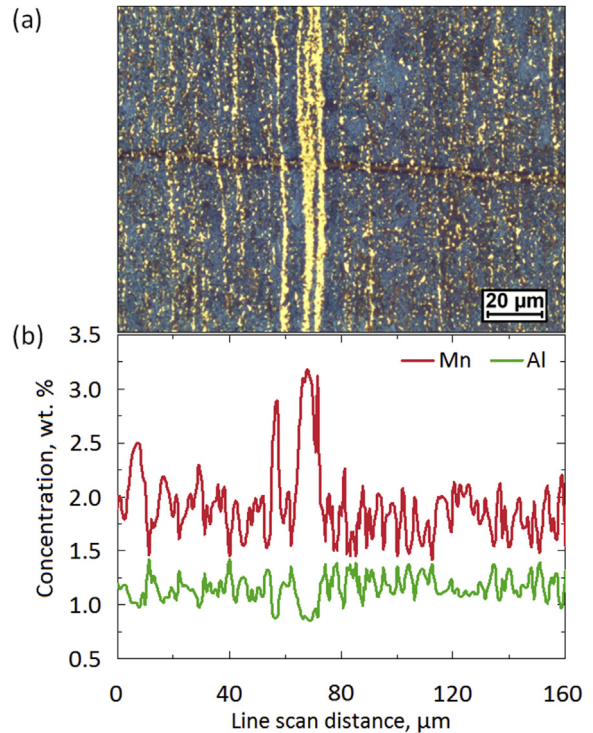


Fig. 6. Elemental line profiles of martensite/austenite bands embedded in the ferrite matrix in the studied steel after cold-rolling and annealing (CRA), showing inverse segregation of aluminium and manganese.

5. Discussion

5.1. Partitioning during casting

Having established that microstructural banding is linked to interdendritic segregation, the next step is to understand the underlying mechanism, and specifically the role of aluminium. Examination of the pseudo-binary equilibrium diagram for the Fe-0.15C-2Mn-0.4Cr-0.4Si-[0–2] Al system shows that the addition of Al widens the peritectic solidification region which will serve to decrease the partition coefficient *i.e.* the ratio of solid to liquid

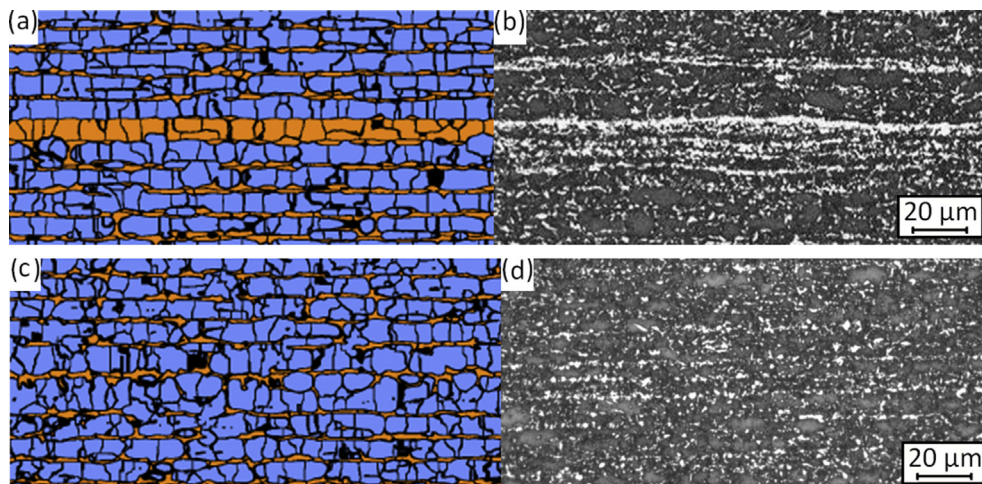


Fig. 5. The microstructures predicted by the CA model in the CRA condition for process conditions to (a) promote or (c) suppress the formation of banding are compared to micrographs of the observed structure as etched using LePera reagent (b and d, respectively), see text.

solubility, thereby increasing segregation, see Fig. 7.

In order to quantify this effect, calculations were carried out for different Al contents and the average calculated partition coefficients of each of the alloying elements are shown in Fig. 8. Fig. 8a shows an increase of bcc phase from 65% to 81% at 2 wt % Al, consistent with a longer cooling trajectory in the liquid + bcc region with increasing Al content. Increasing Al content leads to increased partitioning of Mn, Cr and Si into the liquid, and hence in the resulting fcc phase, with the exception of Al itself which partitions into the bcc.

For the investigated alloy, there is less than 30% liquid remaining at the peritectic temperature. Based on flow velocity calculations during cooling [33] it can be deduced that, given the size of the dendrites, there is little fluid flow in the interdendritic liquid and therefore the bulk concentration should not change during further solidification. Based on this assumption, the composition in the interdendritic region, and hence bands in the final microstructure, should coincide with the composition of the liquid at the peritectic temperature *i.e.* at the point that fcc starts to form. It follows then that the composition of the centre-line band should coincide with the composition of the final liquid to solidify.

The average partition coefficients of the post-bcc liquid and of the final liquid to solidify can thus be calculated, see Table 4. In the same way, the partition coefficient can be estimated as the ratio of the bulk composition to the compositions of each element in bands and at the centre-line of the CRA microstructure. These values are also given in Table 4 and show very good agreement with the model calculation, which further supports the hypothesis that banding is the result of interdendritic segregation.

5.2. Diffusion of aluminium during re-heating

It has long been established that Mn segregation does not homogenise during the reheating times in industrial production due to low diffusion rates. Fisher et al. [25] estimated that it would require 35 h at 1250 °C to reduce the chemical gradient in the interdendritic region to half its original value. Based on the available literature for aluminium diffusion in iron and iron-based alloys, see Table 5 and Fig. 9, Fisher's solution to Fick's law for halving the chemical gradient ranges from seconds to hundreds of hours at 1250 °C, see Table 5, due to the wide variation in the reported values of the diffusion coefficient, D_{Al} , at that temperature [44–50].

Since the evidence shows that aluminium (and also silicon and

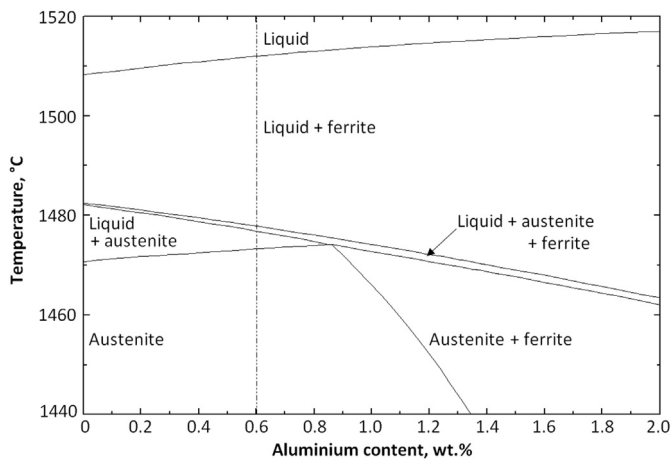


Fig. 7. Pseudo-binary phase diagram of the Fe-0.15C-2Mn-0.4Cr-0.4Si-(x)Al system, where $x = 0-2$ wt %. The vertical dashed line denotes the Al content present in the studied steel.

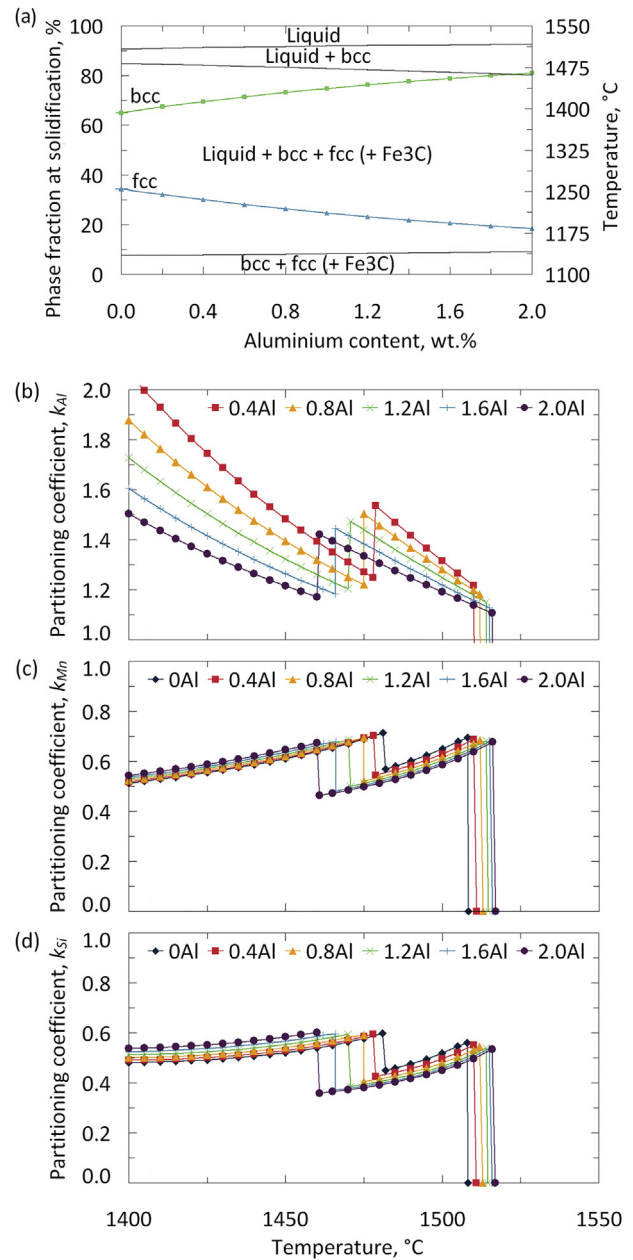


Fig. 8. Effect of aluminium on (a) phase fractions and transformation temperatures, and on the partitioning coefficient of (b) Al, (c) Mn and (d) Si in Fe-0.15C-2Mn-0.4Cr-0.4Si-(x)Al steel, where $x = 0-2$ wt %.

Table 4

Comparison of calculated and experimental values of the partition coefficient in Fe-0.15C-2Mn-0.4Cr-0.4Si-0.6Al.

Element/phase	Calculated		Measured	
	Post-bcc liquid	Final liquid	Bands	Centre-line
Mn	0.95	0.70	0.89 ± 0.04	0.73 ± 0.13
Cr	1.00	0.93	0.95 ± 0.02	0.87 ± 0.07
Si	0.97	0.59	0.88 ± 0.04	0.64 ± 0.16
Al	1.11	1.33	1.11 ± 0.01	1.28 ± 0.06

manganese for that matter) are not homogenised under practical processing conditions, this can only mean that the presence of multiple diffusing species reduces their individual diffusivity. In

Table 5
Reported values of the diffusion parameters for Al in pure iron and iron-based alloys.

Base material	Aluminium composition range, wt%	Temperature range, °C	D_0 , $10^{-4} \text{ m}^2 \text{ s}^{-1}$	Q kJ mol $^{-1}$	Homogenisation time at 1250 °C, s	Reference
bcc-Fe	Not reported	897–1097	5.15	245.8	2561	[46]
bcc-Fe	0–5	920–1210	27.0	188	436	[47] ^a
fcc-Fe (AISI 316L)	Not reported	500–640	5.0	184	170	[49]
ion implanted bcc-Fe	0–8	775–900	1.6	306	1.1×10^6	[45]
0.15C-0.3Mn	0–34	950–1100	30.1	234.5	174	[44]
0.17C-0.5Mn-0.3Si steel (Q235)	Not reported	1020–1080	1.7	142	1.6	[48]

^a Incorrectly attributed to Tobin [50] in *Smithells Metals Reference Book* [47]; the latter reference will be used.

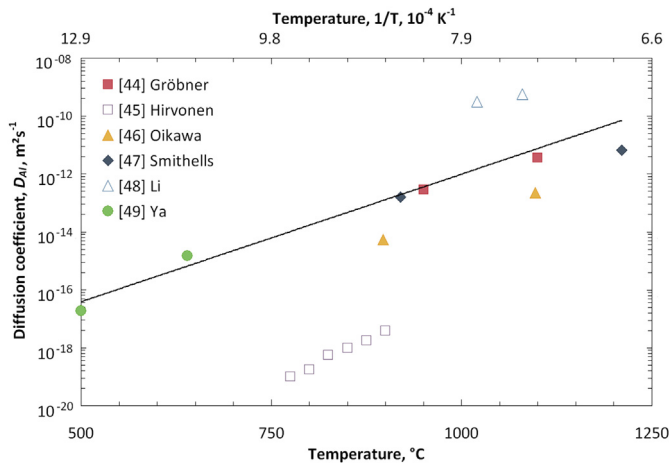


Fig. 9. Temperature dependent diffusion coefficients of Al in pure iron and iron-based alloys. The solid line represents a log-linear fit through the data (except data from Hirvonen [45]).

order to verify this hypothesis, calculations were carried out using the DICTRA software in combination with Thermo-Calc to determine the extent of diffusion in a quaternary system. The resulting step and linear plots in Fig. 10 show that there is limited diffusion of Mn and Al at the boundaries, even after very long processing times. If the minimum criterion for homogenisation can be defined as a halving of the concentration gradient over the diffusion length, then in the case of the step calculations (representing the maximum mobility case) this has been only been achieved for Mn and Al within 10 μm from either side of the interface after almost 28 h at 1250 °C, see Fig. 10 a and b. In contrast, this criterion is fulfilled for the carbon concentration gradient within 100 s, see Fig. 10c.

For the same time and temperature settings, there is no position within the diffusion length of the linear calculation that satisfies the homogenisation criterion for either Al (Fig. 10d) or Mn. Given that the interdendritic space is almost an order of magnitude larger than the simulation cell, we can conclude that there is no significant homogenisation possible in this alloy within practical time constraints of the thermo-mechanical process.

5.3. Effect of segregation on transformation and banding

To understand the mechanism by which segregation drives the tendency towards banding, the effect of local composition on austenite to ferrite transformation during hot-rolling was calculated using the combined computational model described in Sections 3.2 and 3.3. According to this model, when ΔAe_3 increases in magnitude, the transformation from austenite to ferrite is delayed. On the assumption that the carbon content in austenite is constant in the single phase region, areas with a higher Ae_3 will start to

transform to ferrite earlier during cooling (and vice versa during reheating). Since carbon is more soluble in austenite, this phase will become enriched in carbon and eventually transform to pearlite. When the difference between the bands and the bulk increases, so will the tendency towards banding due to partitioning of carbon away from the transformation front *i.e.* a large value of ΔAe_3 will promote the formation of pearlite bands during cooling to the HR condition.

Given that the effect of Al on the transformation temperature is not well documented, an approximation was derived, see the accompanying Data in Brief article [41]. Ae_3 is calculated by summing the relevant coefficients of the approximation. The effect of Al, Si and Mn content on ΔAe_3 at the centre-line of the investigated alloy is shown in Fig. 11. The data represent the differences in ΔAe_3 for each element in turn, whereby the bulk (and hence partitioned) compositions of the other elements remain constant *i.e.* when considering the effect of Al, the nominal alloy concentration is assigned to the bulk Mn, Cr and Si content, from which the segregated concentration and, hence ΔAe_3 can be calculated.

Table 6 shows the effect per wt % of each of the solid solution alloying elements. Al has the greatest negative effect on this parameter by a factor of more than two compared with Mn. This means that Al segregation, even more than Mn, promotes the formation of banding. Even though Al and Si are both ferrite stabilising elements *i.e.* they would both increase Ae_3 , they show an opposite effect on ΔAe_3 in this case. This is due to the opposite partitioning of these elements: Al to the bulk and Si to the bands. Whilst adding Si will tend to reduce the ΔAe_3 , the greater effect of Al on the transformation temperature results in a greater net effect on ΔAe_3 . The effect of Cr on the transformation temperature combined with the low amount of partitioning results in a negligible effect on ΔAe_3 , and whilst being included in the calculation, it is not shown in Fig. 11.

By applying the values for ΔAe_3 to the concentration profile in the CA model, calculations were made for the different cooling and annealing trajectories described in Fig. 1. The resultant HR and CRA microstructures are shown alongside those predicted by the model in Figs. 4 and 5 respectively. In the HR microstructure there is almost no banding evident in the fast cooled microstructure, which is contrast to the prominent banding slow cooled microstructure, especially at the centre line where the composition difference is the greatest, as previously explained. The CA model captures this difference in banding behaviour very well, as can be seen by comparing the images with the real microstructures in Figs. 4 and 5.

Banding is visible in the CRA microstructures of both processing conditions, although the bands visible in the experimentally observed CRA microstructure of the fast cooling (and heating) process are not continuous in the way that those in the slow cooling (and heating) process are, especially at the centre-line. The predicted microstructures from the CA model reflect the reappearance of banding in the fast heating process, although they are more continuous than those of the experimentally observed microstructure. This is due to the cold rolling process not being

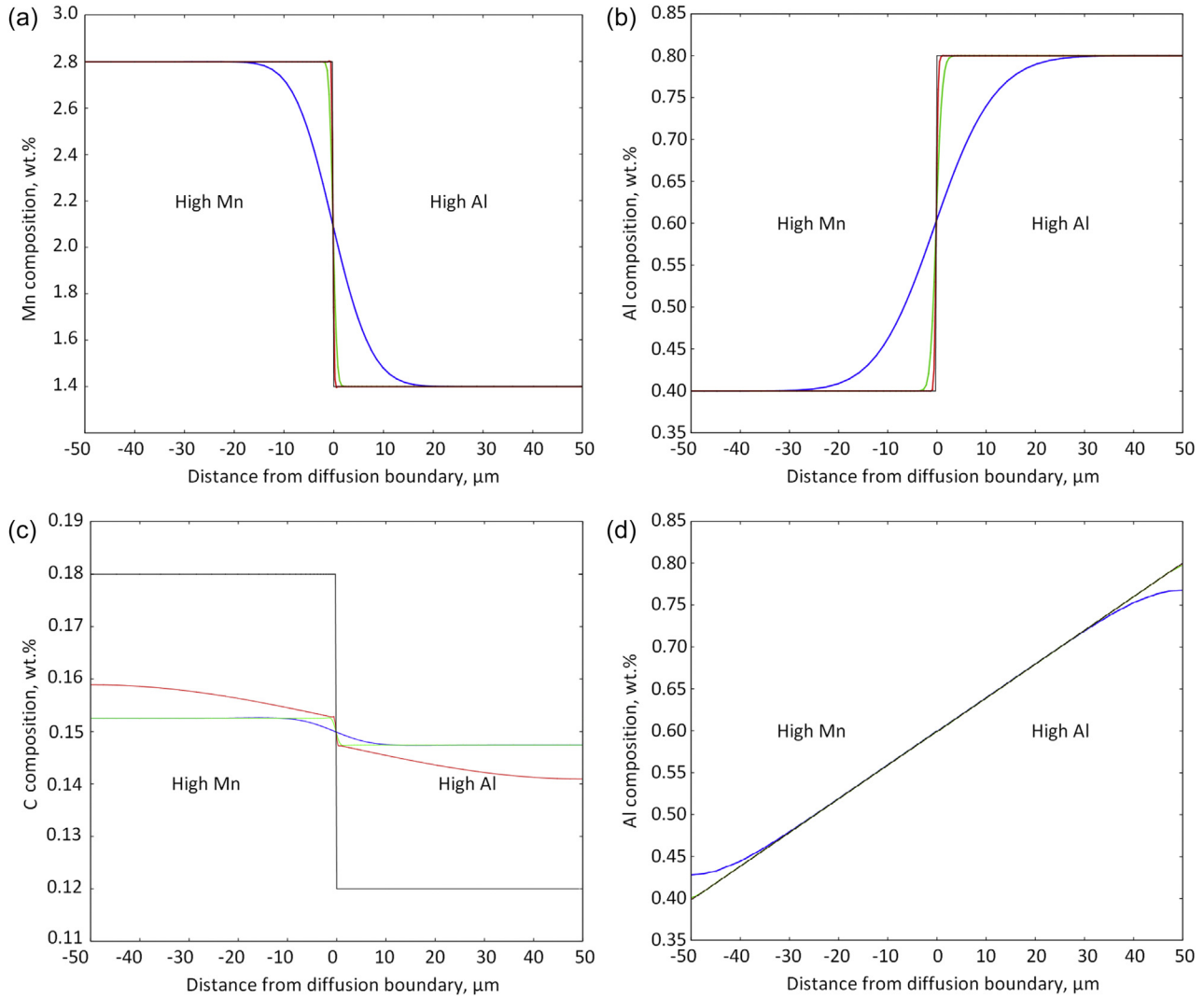


Fig. 10. DICTRA step calculation of (a) Mn, (b) Al and (c) Carbon diffusion at 1250 °C (reheating temperature) and (d) DICTRA linear calculation of Al diffusion under the same conditions. Distributions along the diffusion path/boundary for time steps of 100, 1000 and 100,000 s (28 h) are shown in red, green and blue respectively. (For interpretation of the references to colour in this figure legend, the reader is referred to the web version of this article.)

Table 6

Effect of solid solution alloying elements on the difference in transformation temperature (ΔA_{e3}) between segregated and non-segregated areas in the studied steel grade.

Element	Al	Cr	Mn	Si
Effect on ΔA_{e3} , °C/wt %	-33.7	-3.7	-14.0	+18.9

simulated explicitly. Based on the applied total thickness reduction during cold rolling, the microstructure obtained after hot rolling is scaled accordingly: in this way pearlite and ferrite get the same strain. This means that in the generated cold rolled microstructure the pearlite will be more elongated than in a real microstructure. Although the strain energy contribution is not accounted for, the settings used for the annealing steps result in complete recrystallisation prior to phase transformation and, thus, provide an adequate qualitative description of the microstructure.

6. Conclusions

We have assessed the role of aluminium on the elemental

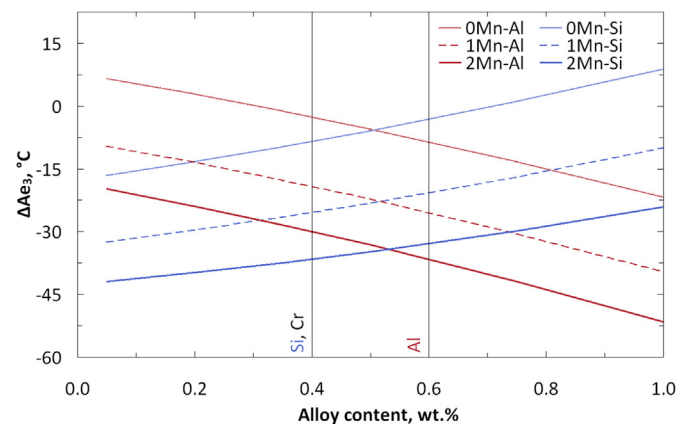


Fig. 11. Effect of Al, Mn and Si concentration on the difference in transformation temperatures between segregated and non-segregated zones (ΔA_{e3}) at the centre-line in the studied steel grade, whereby the nominal alloying contents are represented by the solid vertical lines.

segregation and banding in a TRIP-assisted dual phase steel. Segregation during solidification, the effect of local chemistry on the transformation temperature and the combined effect of transformation and process on band formation were examined and discussed. The conclusions of this study are:

1. Microstructural banding in these steels is characterised by an increased Mn and Si content and a decreased Al content in the second phase. The band at the centre-line is higher in Mn and Si and lower in Al than the other bands. This is the result of different segregation mechanisms during solidification: the band at the centre-line is the result of macro- and microscopic segregation into the final liquid, whereas the other bands are the result only of microscopic segregation in the interdendritic region;
2. Due to its effect upon the Ae_3 transformation temperature, Al has the largest individual contribution of the substitutional alloying elements in these steels on the austenite to ferrite transformation during cooling and, hence, upon banding in multiphase steel;
3. Increasing Al content leads to a marginal increase in partitioning of the other chemical elements into the solid due to widening of the solidification trajectory. Coupled with the counter segregation of Al and Mn, this leads to an increased tendency for banding during hot-rolling, as derived from CA model calculations;
4. Diffusion of solid-state elements during the reheating cycle, particularly aluminium and manganese, is too slow to result in chemical homogenisation. As a result, segregation profiles present after casting remain throughout the down-stream processes and have a significant effect on the final banded microstructure.

Acknowledgements

This work was made possible by the facilities and support of Tata Steel, the Diamond-Manchester Collaboration and the Research Complex at Harwell, funded in part by the EPSRC (EP/I02249X/1). The authors gratefully acknowledge Dr. Marco Rijnders for EPMA analysis, Dr. Kees Bos for the CA model calculations and Mrs. Tu Phan Tran for assistance with the microstructural characterisation. Further thanks are due to Prof. In-Ho Jung at McGill University for assistance with FactSage.

Appendix A. Supplementary data

Supplementary data related to this article can be found at <http://dx.doi.org/10.1016/j.actamat.2016.05.046>.

Author contributions

B.L.E., E.J.-M. and P.D.L. planned the experiments. Steel samples were designed, manufactured and prepared by B.L.E. Thermodynamic calculations and numerical analysis were performed by B.L.E., R.M. and S.B. Microstructural characterisation, image and data analysis was carried out by B.L.E. The manuscript was prepared by B.L.E., E.J.-M., R.M. and P.D.L.

References

- [1] H. Hofmann, D. Mattissen, T.W. Schaumann, Advanced cold rolled steels for automotive applications, *Steel Res. Int.* 80 (2009) 22–28, <http://dx.doi.org/10.1002/srin.200990094>.
- [2] M. Gomez, C.I. Garcia, D.M. Haezebrouck, A.J. DeArdo, Design of composition in (Al/Si)-alloyed TRIP steels, *ISIJ Intl.* 49 (2009) 302–311.
- [3] J.G. Speer, D.K. Matlock, B.C. De Cooman, J.G. Schroth, Carbon partitioning into austenite after martensite transformation, *Acta Mater.* 51 (2003) 2611–2622, [http://dx.doi.org/10.1016/S1359-6454\(03\)00059-4](http://dx.doi.org/10.1016/S1359-6454(03)00059-4).
- [4] A.J. Clarke, J.G. Speer, M.K. Miller, R.E. Hackenberg, D.V. Edmonds, D.K. Matlock, F.C. Rizzo, K.D. Clarke, E. De Moor, Carbon partitioning to austenite from martensite or bainite during the quench and partition (Q&P) process: a critical assessment, *Acta Mater.* 56 (2008) 16–22, <http://dx.doi.org/10.1016/j.actamat.2007.08.051>.
- [5] H. Liu, X. Lu, X. Jin, H. Dong, J. Shi, Enhanced mechanical properties of a hot stamped advanced high-strength steel treated by quenching and partitioning process, *Scr. Mater.* 64 (2011) 749–752.
- [6] J. Tobata, K.L. Ngo-Huynh, N. Nakada, T. Tsuchiyama, S. Takaki, Role of silicon in Q&P treatment of low-carbon martensitic stainless steel, *ISIJ Intl.* 52 (2012) 1377–1382.
- [7] S. Oliver, T.B. Jones, G. Foulrais, Dual phase versus TRIP strip steels: microstructural changes as a consequence of quasi-static and dynamic tensile testing, *Mater. Charact.* 58 (2007) 390–400.
- [8] J. Kobayashi, S.M. Song, K. Sugimoto, Microstructure and retained austenite characteristics of ultra high-strength TRIP-aided martensitic steels, *ISIJ Intl.* 52 (2012) 1124–1129.
- [9] P.J. Jacques, E. Girault, A. Mertens, B. Verlinden, J. Van Humbeeck, F. Delannay, The developments of cold-rolled TRIP-assisted multiphase steels: Al-alloyed TRIP-assisted multiphase steels, *ISIJ Intl.* 41 (2001) 1068–1074.
- [10] J.-Y. Kang, H.-C. Lee, S.H. Han, Effect of Al and Mo on the textures and microstructures of dual phase steels, *Mater. Sci. Eng. A* 530 (2011) 183–190.
- [11] D. San Martín, Y. Palizdar, C. Garcia-Mateo, R.C. Cochrane, R. Brydson, A.J. Scott, Influence of aluminium alloying and heating rate on austenite formation in low carbon-manganese steels, *Metall. Mater. Trans. A* 42 (2011) 2011–2591, <http://dx.doi.org/10.1007/s11661-011-0692-1>.
- [12] H.-L. Wei, G.-Q. Liu, H.-T. Zhao, R.-M. Kang, Hot deformation behavior of two C-Mn-Si based and C-Mn-Al based microalloyed high-strength steels: a comparative study, *Mater. Des.* 50 (2013) 484–490.
- [13] M.E. Glicksman, *Principles of Solidification: an Introduction to Modern Casting and Crystal Growth Concepts*, Springer, New York, 2011. ISBN 978-1-4419-7344-3.
- [14] W. Wang, P.D. Lee, M. McLean, A model of solidification microstructures in nickel-based superalloys - predicting primary dendrite spacing selection, *Acta Mater.* 51 (2003) 2971–2987, [http://dx.doi.org/10.1016/S1359-6454\(03\)00110-1](http://dx.doi.org/10.1016/S1359-6454(03)00110-1).
- [15] W.R. Irving, *Continuous Casting of Steel*, The Institute of Materials, London, 1993.
- [16] M.O. El-Bealy, B.G. Thomas, Prediction of dendrite arm spacing for low alloy steel casting processes, *Metall. Mater. Trans. B* 27 (1996) 689–693, <http://dx.doi.org/10.1007/BF02915668>.
- [17] W.J. Boettinger, S.R. Coriell, A.L. Greer, A. Karma, W. Kurz, M. Rappaz, R. Trivedi, Solidification microstructures: recent developments, future directions, *Acta Mater.* 48 (2000) 43–70, [http://dx.doi.org/10.1016/S1359-6454\(99\)00287-6](http://dx.doi.org/10.1016/S1359-6454(99)00287-6).
- [18] H. Mizukami, K. Hayashi, M. Numata, A. Yamanaka, Prediction of solid-liquid interfacial energy of steel during solidification and control of dendrite arm spacing, *ISIJ Intl.* 52 (2012) 2235–2244.
- [19] P. Wycliffe, Microanalysis of dual phase steels, *Scr. Metall.* 18 (1984) 327–332.
- [20] A.N. Kumar, S.N. Basu, Manganese partitioning and dual-phase characteristics in a microalloyed steel, *J. Mater. Sci.* 26 (1991) 2089–2092.
- [21] D. Chakrabarti, C.L. Davis, M. Strangwood, Development of bimodal grain structures in Nb-containing High-Strength Low-Alloy steels during slab reheating, *Metall. Mater. Trans. A* 39 (2008) 1963–1977.
- [22] J. Black, Modeling the Effects of Chemical Segregation on Phase Transformations in Medium Carbon Bar Steels (MSc thesis), Colorado School of Mines, Golden, CO, USA, 1998.
- [23] L. Tan, Multi-scale Modelling of Solidification of Multi-component Alloys (PhD thesis), Cornell University, Ithaca, NY, USA, 2007.
- [24] E.J. Pickering, Macrosegregation in steel ingots: the applicability of modelling and characterisation techniques, *ISIJ Intl.* 53 (2013) 935–949.
- [25] R.M. Fisher, G.R. Speich, L.J. Cuddy, H. Hu, Phase transformations during steel production, in: *Proceedings of Darken Conference "Physical Chemistry in Metallurgy"*, Monroeville, PA, USA, 1976.
- [26] E. Navara, B. Bengtsson, K.E. Easterling, Austenite formation in manganese partitioning dual-phase steel, *Mater. Sci. Technol.* 2 (1986) 1196–1201.
- [27] Y. Toji, T. Yamashita, K. Nakajima, K. Okuda, H. Matsuda, K. Hasegawa, K. Seto, Effect of Mn partitioning during intercritical annealing on following γ - α transformation and resultant mechanical properties of cold-rolled dual phase steels, *ISIJ Intl.* 51 (2011) 818–825.
- [28] O. Dmitrieva, D. Ponge, G. Inden, J. Millan, P. Choi, J. Sietsma, D. Raabe, Chemical gradients across phase boundaries between martensite and austenite in steel studied by atom probe tomography and simulation, *Acta Mater.* 59 (2011) 364–374.
- [29] M. Kuzmina, D. Ponge, D. Raabe, Grain boundary segregation engineering and austenite reversion turn embrittlement into toughness: example of a 9 wt% medium Mn steel, *Acta Mater.* 86 (2015) 182–192, <http://dx.doi.org/10.1016/j.actamat.2014.12.021>.
- [30] D. De Knijf, M.J. Santofimia, H. Shi, V. Bliznuk, C. Föjler, R. Petrov, W. Xu, In situ austenite-martensite interface mobility study during annealing, *Acta Mater.* 90 (2015) 161–168, <http://dx.doi.org/10.1016/j.actamat.2015.02.040>.
- [31] S.E. Offerman, N.H. van Dijk, M.T. Rekveldt, J. Sietsma, S. van der Zwaag, Ferrite/pearlite band formation in hot rolled medium carbon steel, *Mater. Sci.*

- Technol. 18 (2002) 297–303.
- [32] A. Grajcar, M. Kaminska, M. Opiela, P. Skrzypczyk, B. Grzegorzczak, E. Kalinowska-Ozgowicz, Segregation of alloying elements in thermo-mechanically rolled medium-Mn multiphase steels, *J. Achiev. Mater. Manuf. Eng.* 55 (2012) 256–264.
- [33] S. Karagadde, L. Yuan, N. Shevchenko, S. Eckert, P.D. Lee, 3-D microstructural model of freckle formation validated using in situ experiments, *Acta Mater.* 79 (2014) 168–180, <http://dx.doi.org/10.1016/j.actamat.2014.07.002>.
- [34] C. Bos, M.G. Mecozzi, D.N. Hanlon, M.P. Aarnts, J. Sietsma, Application of a three-dimensional microstructure evolution model to identify key process settings for the production of dual-phase steels, *Metall. Mater. Trans. A* 42 (2011) 3602–3610.
- [35] C. Bos, M.G. Mecozzi, J. Sietsma, A microstructure model for recrystallisation and phase transformation during the dual-phase steel annealing cycle, *Comp. Mater. Sci.* 4 (2010) 692–699.
- [36] F.G. Caballero, A. García-Junceda, C. Capdevila, C. García de Andrés, Evolution of microstructural banding during the manufacturing process of dual phase steels, *Mater. Trans.* 47 (2006) 2269–2276, <http://dx.doi.org/10.2320/matertrans.47.2269>.
- [37] J. Schindelin, I. Arganda-Carreras, E. Frise, Fiji: an open-source platform for biological-image analysis, *Nat. Methods* 9 (2012) 676–682.
- [38] C. Bale, E. Bêlisle, P. Chartrand, S. Deckerov, G. Eriksson, K. Hack, I.H. Jung, Y.-B. Kang, J. Melançon, A. Pelton, C. Robelin, S. Petersen, FactSage thermochemical software and databases - recent developments, *Calphad* 33 (29) (2009).
- [39] K.W. Andrews, Empirical formulae for the calculation of some transformation temperatures, *J. Iron Steel Inst.* 203 (1965) 721–729.
- [40] R.H. Davies, A.T. Dinsdale, J.A. Gisby, MTDATA - thermodynamic and phase equilibrium software from the national physics laboratory, *Calphad* 26 (2002) 229–271, [http://dx.doi.org/10.1016/S0364-5916\(02\)00036-6](http://dx.doi.org/10.1016/S0364-5916(02)00036-6).
- [41] B.L. Ennis, E. Jimenez-Melero, R. Mostert, M.B. Santillana, P.D. Lee, Analytical Approximation of the Ae3 Temperature, 2016. Data in Brief (DIB-D-16-00435).
- [42] A. Borgenstam, A. Engström, L. Häglund, J. Ågren, DICTRA, a tool for simulation of diffusional transformations in alloys, *J. Phase Equilib.* 21 (2000) 269–280.
- [43] A. Engström, L. Höglund, J. Ågren, Computer simulation of diffusion in multiphase system, *Metall. Mater. Trans. A* 25 (1994) 1127–1134.
- [44] P. Gröbner, G.V. Akimova, Koeficient difuze hliníku v železe pro oblast tuhého roztoku, *Hutn. Listy* 10 (1955) 200–202.
- [45] J. Hirvonen, J. Räisänen, Diffusion of aluminium in ion-implanted alpha iron, *J. Appl. Phys.* 53 (1982) 3314–3316.
- [46] H. Oikawa, Review on Lattice Diffusion of Substitutional Impurities in Iron. A Summary Report, Technology Reports, vol. 47, Tohoku University, 1982, pp. 215–223.
- [47] W.F. Gale, T.C. Totemeier, in: *Smithells Metals Reference Book*, eighth ed., Elsevier, 2004.
- [48] Y. Li, J. Wang, Y. Yin, H. Ma, Diffusivity of Al and Fe near the diffusion bonding interface of Fe₃Al with low carbon steel, *Bull. Mater. Sci.* 28 (2005) 69–74.
- [49] W. Ya, Intermetallic Compounds and Intermetallic Layers in AISI316L to Al 1050 Joints (MSc Thesis), Delft University of Technology, The Netherlands, 2011.
- [50] J.M. Tobin, Radio-analysis of krypton and xenon and its use in diffusion experiments with silver, *Acta Metall.* 5 (1957) 398–403, [http://dx.doi.org/10.1016/0001-6160\(57\)90009-3](http://dx.doi.org/10.1016/0001-6160(57)90009-3).